

# 3D Printing as a Rapid Prototyping Approach for Novel RF Cavity Designs

David Sims,<sup>1,2, a)</sup> Benjamin Sims,<sup>1,2,3, b)</sup> Brian Wright,<sup>1</sup> John W. Lewellen,<sup>4</sup> and Sergey V. Baryshev<sup>1,5, c)</sup>

<sup>1)</sup>Department of Electrical and Computer Engineering, Michigan State University, MI 48824, USA

<sup>2)</sup>Department of Physics and Astronomy, Michigan State University, East Lansing, MI 48824, USA

<sup>3)</sup>Facility for Rare Isotope Beams, Michigan State University, East Lansing, MI 48824, USA

<sup>4)</sup>Accelerator Operations and Technology Division, Los Alamos National Laboratory, NM 87545, USA

<sup>5)</sup>Department of Chemical Engineering and Material Science, Michigan State University, MI 48824, USA

3D-printing of radiofrequency (RF) cavity resonators could provide a cost-effective solution that enables rapid prototyping and design flexibility compared to traditional fabrication of full-metal cavities. In this work, the feasibility of fabrication of a useful multi-mode GHz cavity is explored. Two kinds of plastics, two slicing approaches and two metal coating techniques were used to build a series of clamped cavities with thin inner copper surface on otherwise 3D printed plastic surface. The cavities were then bench-tested to identify spatial field distributions, operating frequencies and quality factors ( $Q$ -factor). Pros and cons of the used fabrication approaches were identified and understood, and the performance of longitudinally sliced painted cavity design demonstrated considerable practicality of 3D-printing approach in designing rf systems.

## I. INTRODUCTION

Traditional methods of radiofrequency (RF) cavity fabrication involve the use of high quality solid conductive materials such as oxygen free copper (OFC), to be machined into precise geometries to meet the requirements of their respective high-frequency applications. When bench-testing novel geometries or designs, traditional fabrication methods using OFC materials can quickly become expensive in both time and cost, caused by raw material supply chain and fabrication lead time. Contemporary additive manufacturing, like 3D printing, is capable of producing geometrically complex and accurate designs. Hence, 3D printing could become an alternative fabrication approach offering fast and inexpensive means of experimentally testing and verifying computational cavity designs.

It must be noted that in the field of electron paramagnetic resonance  $TE_{102}$  cavities were previously manufactured as metal-plated glass and plastic structures as early as in the 1950's<sup>1-3</sup>. While those cavities sufficed EPR application, the earlier prototypes were rather simplistic and, by literature review, did not go through basic microwave characterization established around the same time<sup>4</sup> where, at the very least, resonance frequency, quality factor, and field distribution need to be measured. More recently, additive manufacturing has emerged as a cost-effective method for measuring complex permittivity of technologically important liquids such as oils<sup>5,6</sup>. Various clamp-type cavities were reported where the  $Q$ -factor varied anywhere from  $\sim 300$  to 6,000. However, the

reasons behind such a large variation were not given in the corresponding literature.

This study fills these previous gaps and explores the feasibility of a 3D printing approach to fabricate a workable and high-complexity RF cavity that has a novel dual-mode design. Few cavities were printed from two different plastics and copper-coated by two different methods. All cavities were successfully bench-tested and demonstrated, though certain important differences were observed. Cavities final performance were quantitatively compared in terms of electric field distributions and  $Q$ -factors and discussed in detail.

## II. THE CONCEPT OF ADVANCED CAVITY UNDER STUDY

In modern high-brightness RF guns, ultimate attainable electron beam spatio-temporal coherence is constrained between two non-linear forces, i.e. space charge and RF synchronization<sup>7</sup>. To address this basic issue, Serafini *et al.*<sup>8</sup> proposed a multi-mode RF gun that would serve to linearize phase (coordinate-momentum) space of the accelerated electrons. Various computational studies<sup>9-11</sup> proved that multi-mode cavities could potentially reshape and advance the high power RF technology. However, such designs were never realized and vetted in practice, because building and tuning such cavities are practically challenging and require significant time and resources if manufacturing is solely based on OFC technology.

In this work, we consider a cavity that is required to host and individually tune a combination of fundamental  $TM_{010}$  3 GHz and higher-order mode  $TM_{011}$  6 GHz. As schematically illustrated in Fig. 1, individually manipulating with the amplitude and phase of the two modes would allow to linearize the superposition electric field

<sup>a)</sup>Electronic mail: [simsdav4@msu.edu](mailto:simsdav4@msu.edu)

<sup>b)</sup>Electronic mail: [simsben1@msu.edu](mailto:simsben1@msu.edu)

<sup>c)</sup>Electronic mail: [serbar@msu.edu](mailto:serbar@msu.edu)

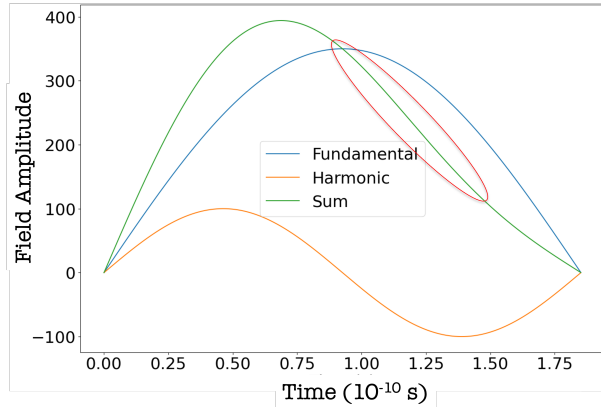


Figure 1: The concept of TM<sub>010</sub> (blue) and TM<sub>011</sub> (orange) superposition highlighting the linearization of the *E*-field.

(shown by red ellipse) hence allowing for linear energy chirp applied to electrons. Such TM<sub>010</sub>/TM<sub>011</sub> cavity would be a beam compression device that does not sacrifice coherence of the beam as compared to the traditional approach used in so-called bunching RF cavities<sup>12</sup>.

### III. DESIGN AND FABRICATION

#### A. Plastics and Printing

The dual-mode cavity was fully designed in COMSOL which included all ports for couplers and tuners. A Stratasys J55 Prime 3D machine was used to print multiple latitudinally and longitudinally sliced tests cavities. VeroUltraWhite RGD824, a photopolymer material, was used as a feedstock material for printing. After printing, the cavities were cured with UV light inside the printer to ensure the material hardened appropriately.

Because interior conductive layer had to be applied on the inner cavity surfaces, to store the electromagnetic energy, required that the cavity be printed in two halves. Two possible options, longitudinal and latitudinal slicing (Fig. 2), were explored. This change in slicing direction aimed to provide insight into how the orientation of the print might influence the overall functionality, which will be explored in greater detail in Section V.

Once printed, the cavities were subjected to two distinct methods of coating the interior with a conductive material. The first method involved sputtering, while the second method used a conductive paint.

As presented in Fig. 3, a total of 3 cavities were successfully fabricated. A fourth cavity was attempted, which utilized a sputtering process on a cavity sliced along the longitudinal axis. However, due to the complex geometry of this cavity, the copper coating was uneven, leading to suboptimal and nonviable results. Namely, the geometry of the nose cones, based on the geometry of the slice

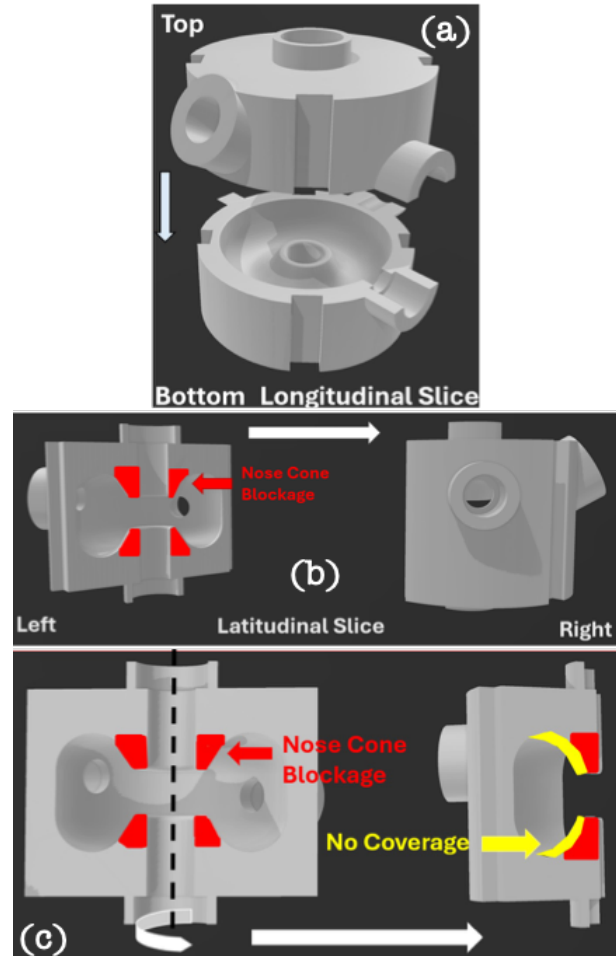


Figure 2: 3D models of two distinct cavity slicing: (a) longitudinal and (b) latitudinal where nose cones blocking sputtering are shown in red. (c) Another rendering of blockade locations due to the complex nose cone geometry.

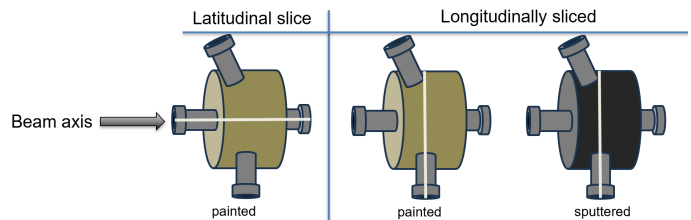


Figure 3: Diagram of the three assembled and tested cavities.

of the cavity (shown in red in Fig. 2), creates pockets with no direct line of sight (shown in yellow), thereby obstructing the sputtering process.

## B. Sputtering Process

The cavities were first cleaned using isopropanol to ensure a grease-free surface. It was then placed into a Denton Vacuum Desktop Pro DC dual-gun sputtering system. The system was pumped down to a base pressure of  $1 \times 10^{-5}$  Torr. Using argon as a working gas, first, a 30 nm layer of titanium was deposited onto the cavity to improve adhesion of the copper layer. Using a calibration curve with a particular ion energy and current, a total of 5  $\mu\text{m}$  of copper had been sputtered. This method ensured that the cavity's conductive coating was much thicker than the skin depth, about 1  $\mu\text{m}$  at 3 and 6 GHz.

## C. Painting Process

The cavities were first cleaned using isopropanol to remove contaminants that could interfere with the painting process. This ensured for more optimal adhesion of the paint to the plastic surface. Once cleaned, the cavity was then dried for 24 hours and prepared for the application of the 842WB Super Shield Water-Based Silver Conductive paint. The first layer of paint was then applied to the inner surface of the cavity using a fine brush, which ensured controlled application. Efforts were made to keep the applied layer as uniform as possible by visual inspection.

This process was repeated three times, each layer was allowed to dry for 30 minutes before the next coat was applied. After the third layer had dried, a final layer of paint was applied around the edges of the cavity to ensure a complete and uniform conductive surface. Following the final application, the cavity was then closed and sealed by joining the two halves and tightening them together using custom clamps. This ensured a secure seal between the two halves. The seal was left to dry for two days to fully cure and bond the two halves of the cavity together. This curing time ensured stability of the conductive layer and the overall integrity of the cavity prior to any testing or further processing.

## IV. CHARACTERIZATION RESULTS

### A. Wire Pull

In order to measure the mode  $E$ -field distributions, localized perturbations were introduced to the electromagnetic field using a short, thin piece of wire attached to a dielectric string and pulled through the cavity along its beam axis. As shown in the diagram in Fig.4, more specifically, a 16-gauge wire, 3 mm in length, was attached to a dielectric string and pulled through the longitudinal axis of the cavity in  $1\text{ cm} \pm 10\text{ mm}$  intervals across all three fabricated 3D-printed cavities. Identical type of measurements were made for both  $\text{TM}_{010}$

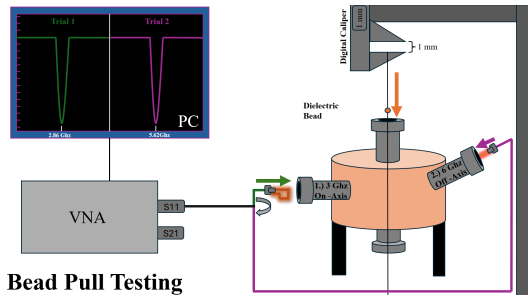


Figure 4: Conceptual diagram of the bead-pull testing setup/procedure.

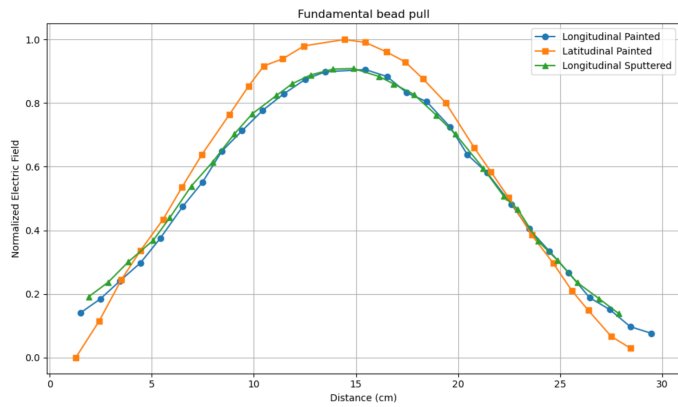
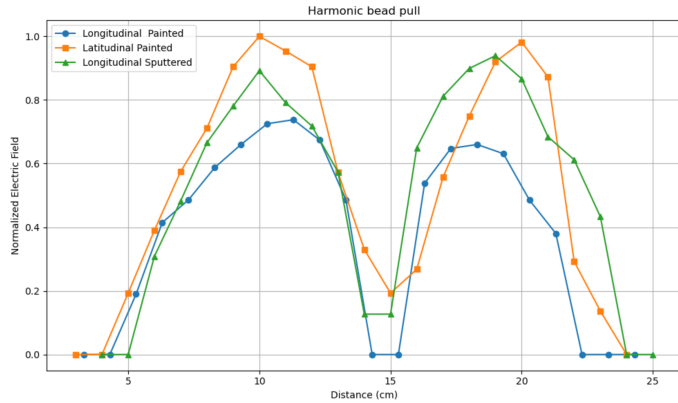
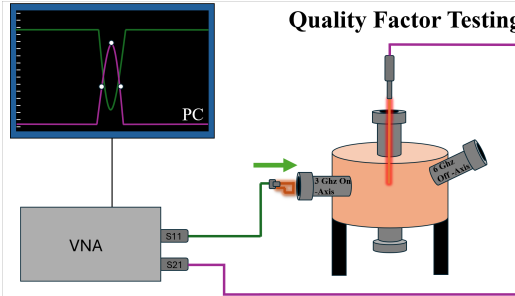
and  $\text{TM}_{011}$  modes. At every position, frequency detuning  $\Delta\omega_{dt}(z)$  along the beam/longitudinal/ $z$ -direction was recorded: the resonant frequency of the cavity mode shifts in proportion to the strength of the  $E$ -field (on-axis,  $z$ -axis,  $\text{TM}$  mode  $H$ -field is negligible) as

$$\Delta\omega_{dt}(z) = \omega(z) - \omega_0 \propto E(z)^2 \omega_0, \quad (1)$$

The wire-pulls successfully demonstrated that the designed and fabricated cavities indeed were able to store both prescribed modes, making them dual-mode cavities.  $\text{TM}_{010}$  and  $\text{TM}_{011}$  modes were successfully excited as can be seen in Fig.5 (fundamental mode) and Fig.6 (harmonic).

### B. Quality Factor

To estimate mode  $Q$ -factors  $S11$  and  $S21$  parameters were measured using a calibrated vector network analyzer (VNA). To ensure minimal power loss between the input transmission line and the cavity, impedance matching was performed using a Smith chart. The input probe ( $S11$ ) was adjusted, and the impedance of the system was plotted on the chart. By manipulating the location of the input probe within the cavity, the impedance point of the cavity was aligned with the  $50\ \Omega$  reference point at the center of the Smith chart. This alignment ensured that the cavity's impedance matched that of the input transmission line, minimizing the reflection coefficient and allowing for maximum energy transfer. A phase diagram was used to then verify critical coupling. As the coupler was adjusted, the phase change as a function of frequency of the transmitted signal was observed. Around the resonant frequency, the phase shift exhibited a  $180^\circ$  change, highlighting the balance between the electric and magnetic fields of the modes thereby additionally confirming critical coupling. At critical coupling, to evaluate  $Q$ -factor the pickup probe (measuring  $S21$  parameter) was inserted to reach into the beam axis of the cavity, as diagrammed in Fig.7. Again, the  $S21$  probe length was optimized to minimize its coupling and therefore cavity perturbation/loading by iteratively changing the probe

Figure 5: Relative  $E$ -field for  $TM_{010}$  mode.Figure 6: Relative  $E$ -field for  $TM_{011}$  mode.Figure 7: Conceptual diagram of the  $Q$ -factor testing setup/procedure.

length such that the width  $\Delta\omega$ , measured -3dB on either side of the  $\omega_0$  of the  $S21$  peak was minimal. After that, so-called loaded  $Q$ -factor ( $Q_L$ ) was calculated as

$$Q_L = \frac{\omega_0}{\Delta\omega}.$$

At minimized loading ( $S21$ ) and critical coupling ( $S11$ ), the coupling factor  $\beta$  is approximately equal to 1. Hence, once  $Q_L$  was determined, the intrinsic quality factor ( $Q_0$ ) was calculated as

$$Q_0 = (1 + \beta)Q_L.$$

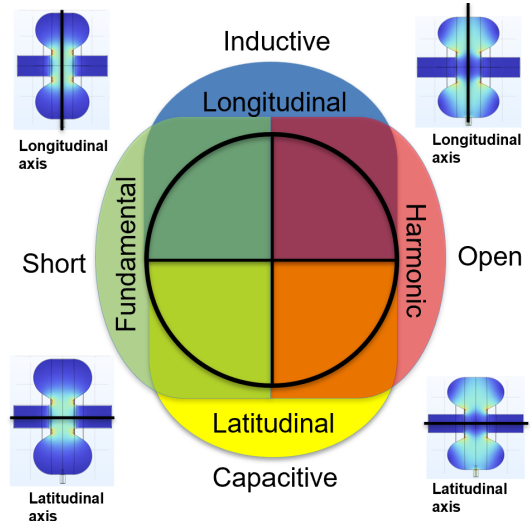


Figure 8: The four quadrants of the Smith chart related to the electric field for both the fundamental and harmonic modes.

All computed  $Q_0$  factors for all three cavities for the both modes are summarized in Table I.

Table I: Comparison of  $Q_0$  for each 3D-printed cavity.

Slicing	longitudinal	latitudinal
Coating	painted	sputtered
$Q_0^{TM010}$	320	623
$Q_0^{TM011}$	336	698

## V. DISCUSSION

Summarizing, among the tested configurations, two relevant trends emerged:

- 1) For the longitudinal case, the sputtered copper coatings yielded superior conductivity and higher  $Q$ -factors relative to silver-painted surfaces. This is despite silver having better conductivity than copper;
- 2) Latitudinal slicing produced  $Q$ -factors up to four times higher than longitudinal slicing. Due to geometrical shadowing, testing of a latitudinally sputtered cavity was not feasible, because it was not possible to deposit copper into the balloon-shaped areas of the cavity (see Fig. 2).

Nevertheless, extrapolating from the current trend suggests that latitudinal slicing with sputtered copper would yield the highest  $Q$ -factor among those studied. Let us now discuss in more detail about how and why material and slicing factors affect  $Q$ -factor metrics.

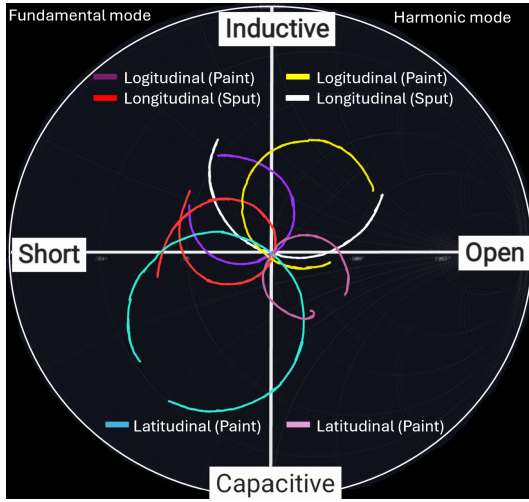


Figure 9: Experimental Smith chart data enhanced for clarity

### A. Geometric Slicing Factor

Enhancement or degradation in cavity performance largely depends on surface current behavior, which in turn is dependent on slicing. The slice direction introduces interruptions along the cavity surface, which result in significant losses. In RF cavities, surface currents  $\vec{J}_s$  flow in the walls within the skin depth, sustaining the magnetic component of a resonant mode. These currents are confined near the surface and can be expressed as  $\vec{J}_s = \hat{t} \times \vec{H}$ , where  $\hat{t}$  is the unit vector tangent to the surface and  $\vec{H}$  is the magnetic field at the conductor boundary. Any structural discontinuity causes both the current  $\vec{J}_s$  to concentrate near the edges of the break and the resistance  $R_s$  at the break. As a result, the power loss per RF cycle rises (thereby degrading  $Q$ -factor) as

$$P_{\text{loss}} \propto R_s \int |\vec{J}_s|^2 dA,$$

where the integral is over the cavity's internal surface area  $A$ . The slice orientation governs how severely these currents are disrupted. Latitudinal slicing tends to preserve the dominant azimuthal current paths for both modes unperturbed. Conversely, longitudinal slicing intersects current flowing regions, causing power loss per RF cycle, therefore reducing  $Q$  from  $\sim 1,400$  to  $\sim 300$ .

Note that both slice directions cause disruptions to the system. Latitudinal slicing predominantly disrupts the electric field structure, while longitudinal slicing disrupts the magnetic field and, hence, the current distribution. These electric or magnetic field-induced current disruptions manifest as distinct impedance signatures on the Smith chart, appearing as capacitive (for latitudinal slicing) or inductive (for longitudinal slicing), respectively.

The coupling method further defines the impedance, as observed on the Smith chart, due to the ratio between

electric and magnetic fields changing for each modes. For a TM mode, the impedance is  $Z = \frac{E}{H}$ . By design, the fundamental mode is excited through coupling to the magnetic field (loop coupler), while the harmonic mode is excited through coupling to the electric field (E-probe). Inductive coupling thus appears at a lower impedance on the Smith chart (smaller  $\frac{E}{H}$  ratio), whereas electrical coupling appears toward higher impedance on the Smith chart (larger  $\frac{E}{H}$  ratio), as shown in Figs. 8, 9 conceptually and experimentally. When considered alongside slice orientation, the coupling strategy enables a quadrant-based segmentation of the Smith chart as shown in Fig. 8. This mapping provides a rapid and intuitive diagnostics for mode identification and verification of critical coupling, as shown in Fig. 9.

### B. Material Factors

The  $Q$  factor of a cavity relates the stored energy  $U$  to  $P_{\text{loss}}$  as

$$Q_0 = \frac{\omega_0 U}{P_{\text{loss}}}. \quad (2)$$

In the presented plastic-based cavities, the conductive coating applied on the inner surfaces determines the conductivity and losses. Losses arise from surface roughness, metal film porosity and physical thickness that must be larger compared to the frequency-dependent skin depth  $\delta = \sqrt{\frac{2}{\mu\sigma\omega_0}}$ .

Silver and copper paints can have two to three orders of magnitude lower conductivity as compared to the bulk silver or copper<sup>13</sup>, thereby requiring more than an order of magnitude thicker coatings, which is hard to control when painted manually. Thus, in addition to having higher  $R_s$  (due to porosity, chemical solution residues, and surface roughness), painted coatings could also be RF leaky. Thin coatings based on vapor deposition are preferred as their conductivity is expected to be closer to that of bulk copper if thickness-uniform deposition is simultaneously possible in such a deposition process. From the comparison presented in Table I, improper coating and slicing can quadruple and double the power loss per RF cycle, respectively.

## VI. CONCLUSIONS AND OUTLOOK

A series of four 3D-printed dual-mode ( $\text{TM}_{010}$  and  $\text{TM}_{011}$ ) cavities were designed, fabricated and tested. Three out of four cavities successfully passed baseline microwave measurements in that they 1) exhibited the fundamental and harmonic fields distribution; 2) resonated near their designed resonant frequencies; 3) could be critically coupled to  $50 \Omega$  line.

At the same time, there were critical lessons learned:

- 1) Even though complex geometries can be printed by the modern 3D printers, one element can overcast another one, thereby making sputtering of the conductive coating challenging or even impossible. This led to one of four printed cavities to fail;
- 2) Slicing is the most critical decision when designing a cavity. It was found that the best results (highest  $Q$ -factors and stronger mode fields) were obtained for the designs in which there were no continuity interruptions to the surface currents supporting particular mode magnetic field distribution. As highlighted in Table I, in the presented case of designing for TM<sub>010</sub> and TM<sub>011</sub> modes, the latitudinal slicing showed, by far, the best cavity performance.
- 3) Lastly, it is highly desired to have a uniform and continuous conductive coating (about 5 skin depths) on the inner cavity surfaces. It is desired to have a pure material deposition (sputtering or electroplating plating) and not water or organic-based paints as conductivity of pure materials coatings is higher and, especially sputtering, are not intrinsically porous or rough as long as the plastic's surface is not porous or rough.

In summary, based on best practices described here, 3D printing of RF cavities appears to be a viable and cost-effective approach for rapid prototyping or light weight cavity fabrication (likely for low and medium power applications).

## VII. ACKNOWLEDGMENTS

The work was supported by the U.S. Department of Energy Office of Science, High Energy Physics under Cooperative Agreement Award No. DE-SC0018362.

## REFERENCES

<sup>1</sup>R. Bennett, P. Hoell, and R. Schwenker, "High-frequency modulation system for the varian epr. spectrometer," *Review of Scientific Instruments* **29**, 659–660 (1958).

- <sup>2</sup>P. Chester, P. Wagner, J. Castle, and G. Conn, "Plastic microwave cavities for epr," *Review of Scientific Instruments* **30**, 1127–1128 (1959).
- <sup>3</sup>P. Cevc, "Plastic epr microwave cavity suitable for modulation at high and low frequencies," *Review of Scientific Instruments* **40**, 515–516 (1969).
- <sup>4</sup>E. L. Ginzton, *Microwave measurements* (New York: McGraw-Hill).
- <sup>5</sup>A. M. Mohammed, A. Hart, J. Wood, Y. Wang, and M. J. Lancaster, "3D printed re-entrant cavity resonator for complex permittivity measurement of crude oils," *Sensors and Actuators A: Physical* **317**, 112477 (2021).
- <sup>6</sup>G. M. Rocco, N. Delmonte, D. Schreurs, S. Marconi, F. Auricchio, and M. Bozzi, ">3D</span> -printed pumpkin-shaped cavity resonator to determine the complex permittivity of liquids," *Microwave and Optical Technology Letters* **63**, 1061–1066 (2021).
- <sup>7</sup>K.-J. Kim, "Rf and space-charge effects in laser-driven rf electron guns," *Nuclear Instruments and Methods in Physics Research Section A: Accelerators, Spectrometers, Detectors and Associated Equipment* **275**, 201–218 (1989).
- <sup>8</sup>L. Serafini, R. Rivolta, and C. Pagani, "Neutralization of the emittance blowup induced by rf time dependent forces in rf guns," *Nuclear Instruments and Methods in Physics Research Section A: Accelerators, Spectrometers, Detectors and Associated Equipment* **318**, 301–307 (1992).
- <sup>9</sup>D. H. Dowell, M. Ferrario, T. Kimura, J. Lewellen, C. Limborg, P. Raimondi, J. F. Schmerge, L. Serafini, T. Smith, and L. Young, "A two-frequency RF photocathode gun," <https://doi.org/10.1016/j.nima.2004.04.078>.
- <sup>10</sup>J. W. Lewellen, "Higher-order mode rf guns," [10.1103/PhysRevSTAB.4.040101](https://doi.org/10.1103/PhysRevSTAB.4.040101).
- <sup>11</sup>J. W. Lewellen and J. Noonan, "Field-emission cathode gating for rf electron guns," [10.1103/PhysRevSTAB.8.033502](https://doi.org/10.1103/PhysRevSTAB.8.033502).
- <sup>12</sup>R. Akre, D. Dowell, P. Emma, J. Frisch, S. Gilevich, G. Hays, P. Hering, R. Iverson, C. Limborg-Deprey, H. Loos, *et al.*, "Commissioning the linac coherent light source injector," *Physical Review Special Topics—Accelerators and Beams* **11**, 030703 (2008).
- <sup>13</sup>X. Zeng, P. He, M. Hu, W. Zhao, H. Chen, L. Liu, J. Sun, and J. Yang, "Copper inks for printed electronics: a review," *Nanoscale* **14**, 16003–16032 (2022).